X-ray Magnetic Circular Dichroism in RuO₂

A. Hariki, Y. Takahashi, and J. Kuneš^{2,3}

¹Department of Physics and Electronics, Graduate School of Engineering,
Osaka Metropolitan University, 1-1 Gakuen-cho, Nakaku, Sakai, Osaka 599-8531, Japan
²Institute for Solid State Physics, TU Wien, 1040 Vienna, Austria
³Department of Condensed Matter Physics, Faculty of Science,
Masaryk University, Kotlářská 2, 611 37 Brno, Czechia

We present numerical simulation of the X-ray magnetic circular dichroism (XMCD) of the $L_{2,3}$ and $M_{2,3}$ edges of Ru in antiferromagnetic RuO₂ using a combination of density functional + dynamical mean-field theory and configuration interaction treatment of Anderson impurity model. We study the dependence of the dichroic spectra on the orientation of the Néel vector and discuss it in the context of altermagnetism. Approximate equivalence between the XMCD spectra for geometries with X-rays propagating parallel and perpendicular to the Néel vector is found and shown to be exact in absence of valence spin-orbit coupling and core-valence multipolar interaction.

I. INTRODUCTION

A metallic compensated magnet RuO_2 has attracted a considerable attention recently. The combination of its rutile structure with an antiparallel ordering of spin moments gives rise to a number of phenomena such as the anomalous Hall effect (AHE) [1–8] or charge-spin conversion effects [9–16], and strongly spin-polarized electronic band structures [2, 6, 9, 15, 17–23], unusual among compensated collinear magnets. Moreover, some of these effects depend on the orientation of the Néel vector \mathbf{L} and may be switched by manipulating it. The name altermagnet [9, 15] was introduced for RuO_2 and similar materials to reflect the alternating spin polarization in the momentum space.

Altermagnetism is a non-relativistic concept, i.e., it relies on the spin rotation SU(2) symmetry in the absence of the spin-orbit coupling (SOC). However, the above transport and charge-excitation effects are possible only if altermagnetic order and SOC are present simultaneously. The SOC thus plays a dual role. On one hand, it allows the altermagnetic order to be detectable through some of the technologically interesting transport effects. On the other hand, it gives rise to magneto-crystalline anisotropy and possibly a weak ferromagnetism with a small net magnetization m. To prove the altermagnetic origin of transport phenomena, e.g., AHE, one must not only measure a finite signal, but also distinguish the altermagnetic contribution associated with L from the contribution due to weak ferromagnetism or possibly the external magnetic field associated with m, which requires a careful quantitative analysis [24].

The X-ray magnetic circular dichroism (XMCD) provides an alternative. The XMCD is an odd magneto-optical effect, which arises from the same anti-symmetric part of the conductivity tensor $\sigma^a = \frac{1}{2}(\sigma - \sigma^T)$ as the valence band phenomena, such as AHE or magneto-optical effects in the visible range and therefore follows the same symmetry rules. However, the XMCD, especially in lighter elements, arises due to the SOC in the core state and is only weakly affected by the valence SOC

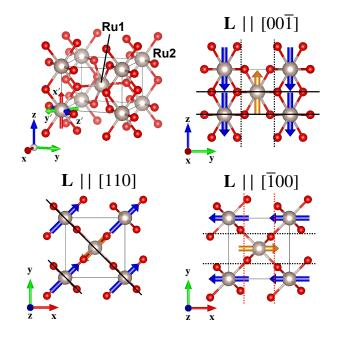


FIG. 1. Crystal structure of RuO_2 and orientations of magnetic structures studied in this work. Solid (dashed) lines indicate the mirror (glide) plane m.

reflecting the typically small orbital moments [25–27]. The theoretical altermagnetic contribution to XMCD can be obtained as the XMCD with the valence SOC switched off. In other words, in the X-ray spectral range it is the core SOC which allows the altermagnetic order to be expressed in the magneto-optical spectra, while the valence SOC, which causes the spurious weak ferromagnetism, has only a marginal contribution [28]. In the optical or transport effects the valence SOC plays a dual role, which cannot be resolved by simply switching it off.

In this article we compute XMCD at $L_{2,3}$ and $M_{2,3}$ edges of Ru for various orientations of the Néel vector **L**. Recently, Sasabe *et al.* [29] calculated XMCD in RuO₂ using the atomic model in an external Zeeman field, and discussed their results in the context of strong-coupling

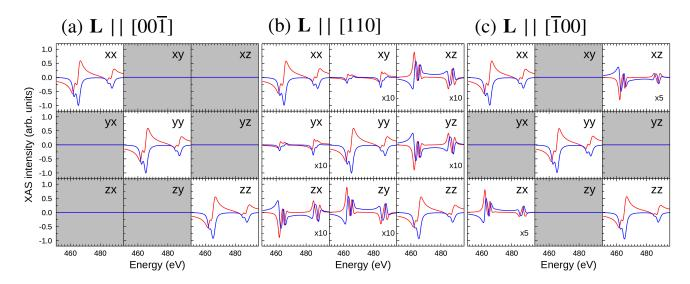


FIG. 2. Real (red) and imaginary (blue) part of the optical conductivity tensor at Ru $M_{2,3}$ edge for different orientations of the Néel vector **L**. Here, the Ru⁴⁺ atomic model (J = 0.50 eV) is used.

(insulator) picture of excitonic magnet [30]. Our calculation of XMCD is performed for the antiferromagnetic metallic state [17] obtained with the density functional plus dynamical mean-field theory (DFT+DMFT) [31–33]. The method identifies a Fermi surface instability as the origin of the antiferromagnetism of metallic RuO₂ [17].

II. COMPUTATIONAL METHOD

Starting with a density functional theory (DFT) calculation for the experimental structure of RuO_2 [34] using Wien2k [35], we construct a multi-band Hubbard model [36, 37] spanning the Ru 4d states. The Ru 4d crystal field levels are summarized in Table I. The electron-electron interaction within the Ru d-shell is parametrized by U=3.0 eV and J=0.45 eV. The interaction parameters affect the magnitude of the ordered Ru moment [17], and thus the XMCD intensities, as examined in the Supplemental Material (SM) [38] (see also references [39–44] therein). We use the same DMFT implementation for the multi-band Hubbard model as in Refs. 45–47. Material-specific details can be found in SM [38].

The XMCD spectra are calculated for i) Ru⁴⁺ atomic model and ii) DMFT + Anderson impurity model (AIM) using the method of Refs. 45–47 based on a configuration interaction impurity solver. The two models implement the same atomic Hamiltonian, which is coupled to an electronic bath via the hybridization function $\Delta(\omega)$ in (ii). The ordered Ru moments are generated by the (self-consistently determined) spin-polarized bath in (ii). In (i) we impose a Zeeman field chosen to generate the same moment as obtained in (ii). Detailed comparison of the two models in SM [38] reveals similar spectra. The com-

putationally cheap atomic model is therefore used for the symmetry analysis of the results.

The SOC is not included in the DMFT self-consistent calculations. However, SOC within the Ru 4d shell is included in the AIM when computing the XMCD intensities. The spin-polarized hybridization densities $\Delta(\omega)$ are transformed to capture the desired Néel vector orientations in these simulatons.

	d_{xy}	$d_{3z^2-r^2}$	$d_{x^2-y^2}$	d_{zx}	d_{yz}
Energy (eV)	3.283	3.522	-0.127	0.036	0.067

TABLE I. The Ru 4d orbital energies in RuO₂ derived from the DFT calculation for the experimental rutile structure. The 4d orbitals are represented in a local coordinate (x'y'z')in the left top panel of Fig. 1.

III. RESULTS

The XMCD is the difference of the absorption spectra for the right-hand and left-hand circularly polarized light propagating along the direction $\hat{\mathbf{k}}$. It is convenient to view the antisymmetric part of the conductivity tensor $\boldsymbol{\sigma}$ as an axial (Hall) vector $\mathbf{h}(\omega) = (\sigma_{zy}^a(\omega), \sigma_{xz}^a(\omega), \sigma_{yx}^a(\omega))$. For simplicity we will not show the ω -dependence from now on, but indicate the dependence on $\hat{\mathbf{k}}$ as well as the orintation of the Néel vector \mathbf{L}

$$\Delta F(\hat{\mathbf{k}}, \mathbf{L}) = F^{+}(\hat{\mathbf{k}}, \mathbf{L}) - F^{-}(\hat{\mathbf{k}}, \mathbf{L}) = 2 \operatorname{Im} \mathbf{h}(\mathbf{L}) \cdot \hat{\mathbf{k}}. \quad (1)$$

The Hall vector $\mathbf{h}(\mathbf{L})$ contains information about XMCD for any direction \mathbf{k} , but depends on the crystallographic orientation of \mathbf{L} . In Fig. 2 we show the elements of $\boldsymbol{\sigma}$

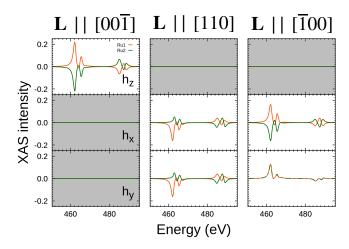


FIG. 3. The imaginary part of the Hall vectors $\mathbf{h}^{(i)}$ at the Ru $M_{2,3}$ -edge for site 1 (yellow) and site 2 (green) obtained for different orientations of the Néel vector \mathbf{L} . Here, the Ru⁴⁺ atomic model (J=0.50 eV) is used. The XMCD spectra of the Ru⁴⁺ atomic model are found in SM [38].

at the Ru $M_{2,3}$ edge for **L** along $[00\bar{1}]$, [110] and $[\bar{1}00]$ directions.

Thanks to the local nature of core-level excitations the observed signal is given by a sum of contributions from the two Ru sites [48]. Depending on the orientation of L, the two Ru sites are connected by some relativistic symmetry operation or not. In the former case XMCD may vanish due to cancellation between the site contributions even if these are non-zero. In the latter case a non-zero XMCD exists if allowed locally by the site symmetry.

A. Symmetry considerations

In the following we will make use of mirror symmetries to discuss the dependence of the XMCD signal, i.e. $\mathbf{h}(\mathbf{L})$ as a function of \mathbf{L} . The mirror (glide) planes are marked in Fig. 1. XMCD is forbidden if there is a mirror plane parallel to x-ray wave vector \mathbf{k} , since it maps the right-hand circular polarization on the left-hand one and vice versa. Since the local moments transform as axial vectors, a crystallographic mirror (glide) plane m is retained as an element of the relativistic symmetry group either if m is parallel to \mathbf{L} and maps the magnetic sublattices on one another or m is perpendicular to \mathbf{L} and maps each magnetic sublattice on itself. Using these simple rules we can understand behavior of the calculated XMCD.

For $\mathbf{L} \parallel [110]$ the two Ru sites are inequivalent. There is no symmetry relationship between the XMCD contributions from the two Ru sites and therefore no cancellation between the site contributions $\mathbf{h}^{(i=1,2)}$ as shown in Fig. 3. The total XMCD signal is non-zero unless XMCD is symmetry-forbidden locally on each site. The mirror plane $m_{(110)}$ maps each Ru site on itself and is perpendicular to the the local moments, which implies that only $\mathbf{h}^{(i)} \parallel [110]$ is allowed.

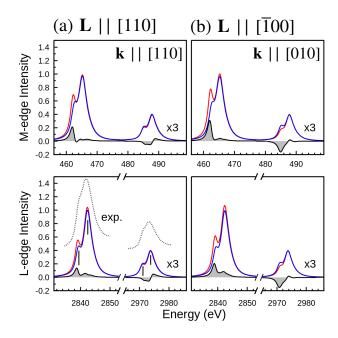


FIG. 4. The XAS calculated for the two circular polarizations (red and blue) at the Ru $M_{2,3}$ -edge (top) and $L_{2,3}$ -edge (bottom) together with the XMCD intensities (shaded) calculated for different orientations of the Néel vector \mathbf{L} and x-ray propagation vector \mathbf{k} using the LDA+DMFT AIM method. The calculated spectral intensities are broadened by Lorentizan of 1.0 eV (HWHM). The experimental L_3 -edge x-ray absorption spectrum is taken from Ref. 49. The L_3 main line and shoulder feature are indicated by vertical lines.

For both $\mathbf{L} \parallel [00\bar{1}]$ and $\mathbf{L} \parallel [\bar{1}00]$ the two Ru sites are equivalent. For $\mathbf{L} \parallel [00\bar{1}]$ the presence of two non-parallel mirror planes, the glide planes $n_{(100)}$ and $n_{(010)}$ mapping the two Ru sites on each other, forbids the total XMCD signal for any direction of \mathbf{k} : $\mathbf{h}^{(1)} = -\mathbf{h}^{(2)}$. Moreover, the mirror plane $m_{(001)}$ implies that $h_x^{(i)} = h_y^{(i)} = 0$ on each site as shown in Fig. 3. For $\mathbf{L} \parallel [\bar{1}00]$, the glide plane $n_{(010)}$ implies $h_z^{(1)} = -h_z^{(2)}$ and $h_x^{(1)} = -h_x^{(2)}$, see Fig. 3. The glide plane $n_{(100)}$, indicated by red dashed lines in Fig. 1, which maps the two Ru sites on each other, must be coupled with the time reversal $n_{(100)}\mathcal{T}$ in order to be a symmetry operation. Therefore the two Ru sites yield the same contribution $h_y^{(1)} = h_y^{(2)}$, see Fig. 3. Finally, we observe that $h_z^{(i)} = 0$ locally thanks to the mirror plane times time-reversal operations $m_{(001)}\mathcal{T}$.

B. L- and M-edge of RuO_2

Fig. 4 shows Ru $L_{2,3}$ - and $M_{2,3}$ -edge absorption spectra with left and right circularly-polarized x-rays and the XMCD intensities calculated using the LDA+DMFT AIM method. The L- and M-edge spectra have similar shapes consisting of a main-peak and a shoulder, indicated by vertical lines [50], and agree well with the the available experimental absorption data on the $M_{2,3}$ -

edges [49]. The shoulders arise from the Ru t_{2g} bands, which host the spin moment. The e_g bands are spin-split but empty. Consequently, the XMCD intensities are largely concentrated in the shoulder for all $M_{2,3}$ - and $L_{2,3}$ -edges. A similar shape of the XMCD spectra was observed on the $M_{2,3}$ -edge XMCD of SrRuO₃, a prototypical ferromagnetic metallic Ru⁴⁺ oxide [51].

Our results show that a non-zero XMCD exists for $L \parallel [110]$ and any k not perpendicular to L as well as $\mathbf{L} \parallel [\bar{1}00]$ and \mathbf{k} not perpendicular to [010]. On the other hand, the XMCD signal vanishes for the experimental easy axis L \parallel [00 $\bar{1}$]. It was shown that L can be tilted in the [110] using external magnetic field [24]. While we have included the valence SOC in calculation of the XMCD spectra using both methods (i) and (ii), we did not include the magnetocrystalline anisotropy in our calculations. Therefore we can only speculate about the external field effect. Looking at the site contributions for the L \parallel [110] in Fig. 3 we observe that site 1 dominates over site 2. Assuming that the external field has only moderate influence on the size of the local moments, we may conclude that it does not alter the present result substantially.

C. No valence SOC, no core-valence multipole interaction

Comparing the XMCD spectra in Fig. 4a and Fig. 4b we observe a similarity pronounced in particular on the L_3 and M_3 edges. In Fig. 5 we show that this is not accidental. In Ref. 28 we have observed that turning off the valence SOC and the multipole part of the core-valence interaction may change the XMCD spectra qualitatively. This is because the Hamiltonian without these interactions possesses a higher symmetry. In the present case, switching off the valence SOC and the multipole part of the core-valence interaction results in equality of the two spectra $\Delta F^{(a)}(\omega) = \Delta F^{(b)}(\omega)$. This may appear surprising given the apparently different geometry in case (a) $\mathbf{k} \parallel \mathbf{L}$ while in case (b) $\mathbf{k} \perp \mathbf{L}$. In Appendix. A we provide an analytic proof, which uses only the presence of two-fold axes along the [110] and [110] directions.

IV. CONCLUSIONS

We have calculated the XMCD spectra on the Ru $L_{2,3}$ and $M_{2,3}$ edges of antiferromagnetic RuO₂ using the LDA+DMFT approach. The present XMCD spectra differ from the recent calculations using the atomic model [29]. The origin of this discrepancy can be traced to different values of the crystal field and Hund's coupling parameters. We have analyzed the symmetry of the XMCD spectra for various orientations of the Néel vector. The results apply to any collinear antiferromagnet with the rutile structure. No XMCD is allowed for the easy axis [001] orientation of the Néel vector \mathbf{L} . We

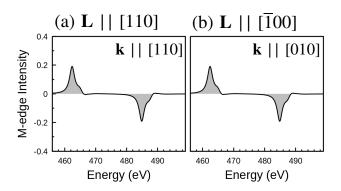


FIG. 5. Ru $M_{2,3}$ -edge XMCD intensities $\Delta F^{(a)}$ in case (a) and $\Delta F^{(b)}$ in case (b) calculated without SOC within the Ru 4d shell and 3p–4d core-valence multiplet interaction for the two different Néel vectors \mathbf{L} and x-ray propagation vectors $\hat{\mathbf{k}}$ by the LDA+DMFT AIM method.

have predicted the XMCD spectra for the experimentally accessible [110] orientation.

ACKNOWLEDGMENTS

We thank Andriy Smolyanyuk and Anna Kauch for discussions and critical reading of the manuscript. This work was supported by JSPS KAKENHI Grant Numbers 21K13884, 21H01003, 23K03324, 23H03817 (A.H.), and by the project Quantum materials for applications in sustainable technologies (QM4ST), funded as project No. CZ.02.01.01/00/22_008/0004572 by Programme Johannes Amos Commenius, call Excellent Research (J.K.).

Appendix A: XMCD with no core-valence exchange and no valence SOC

Here we prove analytically the numerical results of Fig. 4. We start with several definitions. The circular dichroism $\Delta F(\hat{\mathbf{k}}, \mathbf{L}) = F^+(\hat{\mathbf{k}}, \mathbf{L}) - F^-(\hat{\mathbf{k}}, \mathbf{L})$ is the difference of the absorption spectra for the right-hand and left-hand circularly polarized light can be obtained from the Fermi golden rule

$$F^{\pm}(\hat{\mathbf{k}}, \mathbf{L}) = \sum_{f} \left| \left\langle f_{\mathbf{L}} | \hat{T}_{\hat{\mathbf{k}}}^{\pm} | i_{\mathbf{L}} \right\rangle \right|^{2} \delta\left(\omega - E_{fi; \mathbf{L}}\right). \tag{A1}$$

Here $|i_{\mathbf{L}}\rangle$ and $|f_{\mathbf{L}}\rangle$ are the eigenstates of the Hamiltonian, $E_{fi;\mathbf{L}}$ is the excitation energy, and $\hat{T}^{\pm}_{\hat{\mathbf{k}}}$ are the dipole operators for the right- and left-hand polarization with respect to propagation vector $\hat{\mathbf{k}}$. Thanks to the immobility of the core hole the x-ray absorption spectrum is an sum over site contributions.

We will use the geometry of Fig. 6 with the x-rays coming along the x-axis and the quantization z-axis of spin and angular momenta parallel to the crystallographic c-axes. To evaluate XMCD $\Delta F^{(a)}$ and $\Delta F^{(b)}$ for the ge-

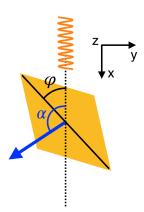


FIG. 6. Geometry used to prove the equality of $\Delta F^{(a)}$ and $\Delta F^{(b)}$ numerically observed in Fig. 4. The Ru atom is located in the center, the parallelogram (long axis parallel to [110]) represents the orientation of the crystal.

ometries for Fig. 4a and Fig. 4b we will vary the angles φ (orientation of the crystal) and α (orientation of the local moment)

$$\Delta F^{(a)} = \frac{1}{2} \left(\Delta F(0,0) + \Delta F(\frac{\pi}{2}, \pi) \right)$$

$$\Delta F^{(b)} = \Delta F(\frac{\pi}{4}, \frac{\pi}{2}).$$
(A2)

Here we use the angles φ and α in $\Delta F(\varphi, \alpha)$ to represent $\hat{\mathbf{k}}$ and \mathbf{L} in the geometry of Fig. 6. Using the relations between the dipole operators \hat{T}^x , \hat{T}^y and \hat{T}^z

$$T^{+} = -T^{x} - iT^{y}$$

$$T^{-} = -T^{x} + iT^{y}$$

$$T^{0} = T^{z}.$$

we express the dipole operators $T_{\hat{x}}^{\pm}$ for the circularly polarizated light propagating along the x-axis, helicity basis for $\hat{\mathbf{k}} \parallel x$, using dipole operators in the helicity basis for $\hat{\mathbf{k}} \parallel z[52]$

$$T_{\hat{x}}^{\pm} = -T^y \mp iT^z = i\left(\frac{T^+ - T^-}{2} \pm T^0\right).$$

The expression (A1) for XMCD then takes the form

$$\Delta F(\varphi, \alpha) = \sum_{f} \left\langle f_{\varphi, \alpha} | \hat{T}^{+} - \hat{T}^{-} | i_{\varphi, \alpha} \right\rangle \left\langle i_{\varphi, \alpha} | \hat{T}^{0} | f_{\varphi, \alpha} \right\rangle$$

$$\times \delta \left(\omega - E_{fi} \right) + c.c.$$

$$\equiv (T^{+} - T^{-}) \overline{T^{0}} + c.c.$$
(A3)

Here, the polarization of the dipole operators is taken with respect to the z-axis. We will use the shorthand notation for the matrix elements of the dipole operators shown on the third line from now on. In absence of the valence SOC and core-valence multipole interaction, the

excitation energy does not depend on the orientation of \mathbf{L} , i.e., the angle α and the eigenstates for arbitrary angles φ and α can be obtained from those for $\varphi=0$ and $\alpha=0$ by a joint z-axis rotation $\mathcal{C}(\varphi,\alpha)$ of core spin, core orbitals and valence orbitals by angle φ and rotation of valence spin by angle α , which transform the operators

$$\mathcal{C}(\varphi,\alpha):d_{ms}\to e^{im\varphi}e^{i\sigma\alpha}d_{m\sigma},\quad p_{m\sigma}\to e^{i(m+\sigma)\varphi}p_{m\sigma},$$

where m is the orbital and $\sigma = \pm \frac{1}{2}$ the spin projection along the z-axis. Next, we use

$$\left\langle \mathcal{C}(\varphi,\alpha)f|\hat{T}|\mathcal{C}(\varphi,\alpha)i\right\rangle = \left\langle f|\mathcal{C}^{-1}(\varphi,\alpha)\hat{T}\mathcal{C}(\varphi,\alpha)|i\right\rangle$$

to transform the dipole operators instead of wave functions in (A3). Using the definition of the dipole operators

$$\hat{T}^{\pm} \equiv \hat{T}^{\pm}_{\uparrow} + \hat{T}^{\pm}_{\downarrow} = \sum_{m,\sigma} \Gamma_{\pm m} \hat{d}^{\dagger}_{m\pm 1\sigma} \hat{p}_{m\sigma}$$
$$\hat{T}^{0} \equiv \hat{T}^{0}_{\uparrow} + \hat{T}^{0}_{\downarrow} = \sum_{m,\sigma} \Gamma^{(0)}_{m} \hat{d}^{\dagger}_{m\sigma} \hat{p}_{m\sigma},$$

we arrive at their transformation properties

$$\mathcal{C}^{-1}(\varphi,\alpha)\hat{T}_{\sigma}^{+}\mathcal{C}(\varphi,\alpha) = e^{i\varphi}e^{-i\sigma(\varphi-\alpha)}\hat{T}_{\sigma}^{+}$$

$$\mathcal{C}^{-1}(\varphi,\alpha)\hat{T}_{\sigma}^{-}\mathcal{C}(\varphi,\alpha) = e^{-i\varphi}e^{-i\sigma(\varphi-\alpha)}\hat{T}_{\sigma}^{-}$$

$$\mathcal{C}^{-1}(\varphi,\alpha)\hat{T}_{\sigma}^{0}\mathcal{C}(\varphi,\alpha) = e^{-i\sigma(\varphi-\alpha)}\hat{T}_{\sigma}^{0}.$$
(A4)

Substituting these into (A3) we get the formula for the XMCD spectra for general angles φ and α

$$\begin{split} \Delta F(\varphi,\alpha) = & (e^{i\varphi}T_{\uparrow}^{+} - e^{-i\varphi}T_{\uparrow}^{-})\overline{T_{\uparrow}^{0}} \\ & + (e^{i\varphi}T_{\downarrow}^{+} - e^{-i\varphi}T_{\downarrow}^{-})\overline{T_{\downarrow}^{0}} \\ & + (e^{i\alpha}T_{\uparrow}^{+} - e^{-i(2\varphi-\alpha)}T_{\uparrow}^{-})\overline{T_{\downarrow}^{0}} \\ & + (e^{i(2\varphi-\alpha)}T_{\downarrow}^{+} - e^{-i\alpha}T_{\downarrow}^{-})\overline{T_{\uparrow}^{0}} + c.c. \end{split} \tag{A5}$$

$$= & (e^{i\alpha}T_{\uparrow}^{+} - e^{-i(2\varphi-\alpha)}T_{\uparrow}^{-})\overline{T_{\downarrow}^{0}} \\ & + (e^{i(2\varphi-\alpha)}T_{\downarrow}^{+} - e^{-i\alpha}T_{\downarrow}^{-})\overline{T_{\uparrow}^{0}} + c.c. \end{split}$$

The $\uparrow\uparrow$ and $\downarrow\downarrow$ terms do not change sign under the magnetic moment reversal $\alpha \to \alpha + \pi$ and thus must vanish the expression for XMCD.

Now we can evaluate the XMCD spectra for the orientations in (A2)

$$\begin{split} \Delta F(0,0) &= (T_{\uparrow}^+ - T_{\uparrow}^-) \overline{T_{\downarrow}^0} + (T_{\downarrow}^+ - T_{\downarrow}^-) \overline{T_{\uparrow}^0} + c.c. \\ \Delta F(\frac{\pi}{2},\pi) &= (-T_{\uparrow}^+ - T_{\uparrow}^-) \overline{T_{\downarrow}^0} + (T_{\downarrow}^+ + T_{\downarrow}^-) \overline{T_{\uparrow}^0} + c.c. \\ \Delta F(\frac{\pi}{4},\frac{\pi}{2}) &= (iT_{\uparrow}^+ - T_{\uparrow}^-) \overline{T_{\downarrow}^0} + (T_{\downarrow}^+ + iT_{\downarrow}^-) \overline{T_{\uparrow}^0} + c.c. \end{split} \tag{A6}$$

Note that this is not enough to guarantee $\Delta F^{(a)} = \Delta F^{(b)}$. We use the fact that in the rutile structure there are two-fold rotation axes parallel to [110] and [1 $\bar{1}$ 0], i.e., $\varphi = 0$ and $\varphi = \frac{\pi}{2}$. In Ref. 28 we have shown that such rotation symmetry implies vanishing of XMCD for the

magnetic moment perpendicular to the X-ray propagation vector, i.e.,

$$\begin{split} &\Delta F(0,\tfrac{\pi}{2}) = \\ &(iT_{\uparrow}^+ - iT_{\uparrow}^-)\overline{T_{\downarrow}^0} + (-iT_{\downarrow}^+ + iT_{\downarrow}^-)\overline{T_{\uparrow}^0} + c.c. = 0 \\ &\Delta F(\tfrac{\pi}{2},\tfrac{\pi}{2}) = \\ &(iT_{\uparrow}^+ + iT_{\uparrow}^-)\overline{T_{\downarrow}^0} + (iT_{\downarrow}^+ + iT_{\downarrow}^-)\overline{T_{\uparrow}^0} + c.c. = 0. \end{split}$$

Adding the two lines we get

$$iT_{\uparrow}^{+}\overline{T_{\downarrow}^{0}} + iT_{\downarrow}^{-}\overline{T_{\uparrow}^{0}} + c.c. = 0,$$
 (A7)

and substituting (A7) into the third line of (A6) concludes the proof

$$\begin{split} \frac{1}{2} \left(\Delta F(0,0) + \Delta F(\frac{\pi}{2},\pi) \right) &= -T_{\uparrow}^{-} \overline{T_{\downarrow}^{0}} + T_{\downarrow}^{+} \overline{T_{\uparrow}^{0}} + c.c. \\ &= \Delta F(\frac{\pi}{4},\frac{\pi}{2}) \end{split}$$

- L. Šmejkal, A. H. MacDonald, J. Sinova, S. Nakatsuji, and T. Jungwirth, Anomalous Hall antiferromagnets, Nat. Rev. Mater. 7, 482 (2022).
- [2] L. Šmejkal, R. González-Hernández, T. Jungwirth, and J. Sinova, Crystal time-reversal symmetry breaking and spontaneous Hall effect in collinear antiferromagnets, Sci. Adv. 6, eaaz8809 (2020).
- [3] K. Samanta, M. Ležaić, M. Merte, F. Freimuth, S. Blügel, and Y. Mokrousov, Crystal Hall and crystal magnetooptical effect in thin films of SrRuO₃, J. Appl. Phys. 127, 213904 (2020).
- [4] M. Naka, S. Hayami, H. Kusunose, Y. Yanagi, Y. Motome, and H. Seo, Anomalous Hall effect in κ-type organic antiferromagnets, Phys. Rev. B 102, 075112 (2020).
- [5] S. Hayami and H. Kusunose, Essential role of the anisotropic magnetic dipole in the anomalous Hall effect, Phys. Rev. B 103, L180407 (2021).
- [6] I. I. Mazin, K. Koepernik, M. D. Johannes, R. González-Hernández, and L. Šmejkal, Prediction of unconventional magnetism in doped FeSb₂, Proc. Natl. Acad. Sci. U.S.A. 118, e2108924118 (2021).
- [7] R. D. Gonzalez Betancourt, J. Zubáč, R. Gonzalez-Hernandez, K. Geishendorf, Z. Šobáň, G. Springholz, K. Olejník, L. Šmejkal, J. Sinova, T. Jungwirth, S. T. B. Goennenwein, A. Thomas, H. Reichlová, J. Železný, and D. Kriegner, Spontaneous anomalous Hall effect arising from an unconventional compensated magnetic phase in a semiconductor, Phys. Rev. Lett. 130, 036702 (2023).
- [8] M. Naka, Y. Motome, and H. Seo, Anomalous Hall effect in antiferromagnetic perovskites, Phys. Rev. B 106, 195149 (2022).
- [9] L. Šmejkal, J. Sinova, and T. Jungwirth, Emerging research landscape of altermagnetism, Phys. Rev. X 12, 040501 (2022).
- [10] M. Naka, S. Hayami, H. Kusunose, Y. Yanagi, Y. Motome, and H. Seo, Spin current generation in organic antiferromagnets, Nat. Commun. 10, 4305 (2019).
- [11] R. González-Hernández, L. Šmejkal, K. Výborný, Y. Yahagi, J. Sinova, T. c. v. Jungwirth, and J. Železný, Efficient electrical spin splitter based on nonrelativistic collinear antiferromagnetism, Phys. Rev. Lett. 126, 127701 (2021).
- [12] M. Naka, Y. Motome, and H. Seo, Perovskite as a spin current generator, Phys. Rev. B 103, 125114 (2021).
- [13] H.-Y. Ma, M. Hu, N. Li, J. Liu, W. Yao, J.-F. Jia, and J. Liu, Multifunctional antiferromagnetic materials with

- giant piezomagnetism and noncollinear spin current, Nat. Commun. 12, 2846 (2021).
- [14] L. Šmejkal, A. B. Hellenes, R. González-Hernández, J. Sinova, and T. Jungwirth, Giant and tunneling magnetoresistance in unconventional collinear antiferromagnets with nonrelativistic spin-momentum coupling, Phys. Rev. X 12, 011028 (2022).
- [15] L. Šmejkal, J. Sinova, and T. Jungwirth, Beyond conventional ferromagnetism and antiferromagnetism: A phase with nonrelativistic spin and crystal rotation symmetry, Phys. Rev. X 12, 031042 (2022).
- [16] S. W. Lovesey, D. D. Khalyavin, and G. van der Laan, Magnetic properties of RuO₂ and charge-magnetic interference in bragg diffraction of circularly polarized X-rays, Phys. Rev. B 105, 014403 (2022).
- [17] K.-H. Ahn, A. Hariki, K.-W. Lee, and J. Kuneš, Antiferromagnetism in ${\rm RuO_2}$ as d-wave Pomeranchuk instability, Phys. Rev. B **99**, 184432 (2019).
- [18] S. Hayami, Y. Yanagi, and H. Kusunose, Momentum-dependent spin splitting by collinear antiferromagnetic ordering, J. Phys. Soc. Jpn. 88, 123702 (2019).
- [19] L.-D. Yuan, Z. Wang, J.-W. Luo, E. I. Rashba, and A. Zunger, Giant momentum-dependent spin splitting in centrosymmetric low-Z antiferromagnets, Phys. Rev. B 102, 014422 (2020).
- [20] L.-D. Yuan, Z. Wang, J.-W. Luo, and A. Zunger, Prediction of low-Z collinear and noncollinear antiferromagnetic compounds having momentum-dependent spin splitting even without spin-orbit coupling, Phys. Rev. Mater. 5, 014409 (2021).
- [21] S. Hayami, Y. Yanagi, and H. Kusunose, Bottom-up design of spin-split and reshaped electronic band structures in antiferromagnets without spin-orbit coupling: Procedure on the basis of augmented multipoles, Phys. Rev. B 102, 144441 (2020).
- [22] P. Liu, J. Li, J. Han, X. Wan, and Q. Liu, Spin-group symmetry in magnetic materials with negligible spinorbit coupling, Phys. Rev. X 12, 021016 (2022).
- [23] J. Yang, Z.-X. Liu, and C. Fang, Symmetry invariants and classes of quasi-particles in magnetically ordered systems having weak spin-orbit coupling, arXiv:2105.12738.
- [24] Z. Feng, X. Zhou, L. Šmejkal, L. Wu, Z. Zhu, H. Guo, R. González-Hernández, X. Wang, H. Yan, P. Qin, X. Zhang, H. Wu, H. Chen, Z. Meng, L. Liu, Z. Xia, J. Sinova, T. Jungwirth, and Z. Liu, An anomalous Hall effect in altermagnetic ruthenium dioxide, Nature Electronics 5, 735 (2022).

- [25] B. T. Thole, P. Carra, F. Sette, and G. van der Laan, X-ray circular dichroism as a probe of orbital magnetization, Phys. Rev. Lett. 68, 1943 (1992).
- [26] D. Weller, J. Stöhr, R. Nakajima, A. Carl, M. G. Samant, C. Chappert, R. Mégy, P. Beauvillain, P. Veillet, and G. A. Held, Microscopic origin of magnetic anisotropy in Au/Co/Au probed with X-ray magnetic circular dichroism, Phys. Rev. Lett. 75, 3752 (1995).
- [27] J. Kuneš and P. M. Oppeneer, Anisotropic X-ray magnetic linear dichroism at the L_{2,3} edges of cubic Fe, Co, and Ni: Ab initio calculations and model theory, Phys. Rev. B 67, 024431 (2003).
- [28] A. Hariki, T. Yamaguchi, D. Kriegner, K. W. Edmonds, P. Wadley, S. S. Dhesi, G. Springholz, V. Šmejkal, K. Výborný', T. Jungwirth, and J. Kuneš, X-ray magnetic circular dichroism in altermagnetic α-MnTe (2023), arXiv:2305.03588.
- [29] N. Sasabe, M. Mizumaki, T. Uozumi, and Y. Yamasaki, Ferroic order for anisotropic magnetic dipole term in collinear antiferromagnets of $(t_{2g})^4$ system, Phys. Rev. Lett. **131**, 216501 (2023).
- [30] G. Khaliullin, Excitonic magnetism in Van Vleck type d^4 mott insulators, Phys. Rev. Lett. **111**, 197201 (2013).
- [31] W. Metzner and D. Vollhardt, Correlated lattice fermions in $d = \infty$ dimensions, Phys. Rev. Lett. **62**, 324 (1989).
- [32] A. Georges, G. Kotliar, W. Krauth, and M. J. Rozenberg, Dynamical mean-field theory of strongly correlated fermion systems and the limit of infinite dimensions, Rev. Mod. Phys. 68, 13 (1996).
- [33] G. Kotliar, S. Y. Savrasov, K. Haule, V. S. Oudovenko, O. Parcollet, and C. A. Marianetti, Electronic structure calculations with dynamical mean-field theory, Rev. Mod. Phys. 78, 865 (2006).
- [34] T. Berlijn, P. C. Snijders, O. Delaire, H.-D. Zhou, T. A. Maier, H.-B. Cao, S.-X. Chi, M. Matsuda, Y. Wang, M. R. Koehler, P. R. C. Kent, and H. H. Weitering, Itinerant antiferromagnetism in RuO₂, Phys. Rev. Lett. 118, 077201 (2017).
- [35] P. Blaha, K. Schwarz, G. Madsen, D. Kvasnicka, and J. Luitz, WIEN2k, An Augmented Plane Wave + Local Orbitals Program for Calculating Crystal Properties (Karlheinz Schwarz, Techn. Universitat Wien, Austria, 2001), ISBN 3-9501031-1-2.
- [36] J. Kuneš, R. Arita, P. Wissgott, A. Toschi, H. Ikeda, and K. Held, Wien2wannier: From linearized augmented plane waves to maximally localized Wannier functions, Comput. Phys. Commun. **181**, 1888 (2010).
- [37] A. A. Mostofi, J. R. Yates, G. Pizzi, Y.-S. Lee, I. Souza, D. Vanderbilt, and N. Marzari, An updated version of wannier90: A tool for obtaining maximally-localised Wannier functions, Comput. Phys. Commun. 185, 2309 (2014).
- [38] See Supplementary Material for details at ...

- [39] M. Matsubara, T. Uozumi, A. Kotani, Y. Harada, and S. Shin, Polarization dependence of resonant X-ray emission spectra in early transition metal compounds, J. Phys. Soc. Jpn. 69, 1558 (2000).
- [40] X. Wang, E. Gull, L. de' Medici, M. Capone, and A. J. Millis, Antiferromagnetism and the gap of a mott insulator: Results from analytic continuation of the self-energy, Phys. Rev. B 80, 045101 (2009).
- [41] L. Boehnke, H. Hafermann, M. Ferrero, F. Lechermann, and O. Parcollet, Orthogonal polynomial representation of imaginary-time Green's functions, Phys. Rev. B 84, 075145 (2011).
- [42] H. Hafermann, K. R. Patton, and P. Werner, Improved estimators for the self-energy and vertex function in hybridization-expansion continuous-time quantum monte carlo simulations, Phys. Rev. B 85, 205106 (2012).
- [43] P. Werner, A. Comanac, L. de' Medici, M. Troyer, and A. J. Millis, Continuous-time solver for quantum impurity models, Phys. Rev. Lett. 97, 076405 (2006).
- [44] M. Jarrell and J. Gubernatis, Bayesian inference and the analytic continuation of imaginary-time quantum monte carlo data, Phys. Rep. 269, 133 (1996).
- [45] A. Hariki, T. Uozumi, and J. Kuneš, LDA+DMFT approach to core-level spectroscopy: Application to 3d transition metal compounds, Phys. Rev. B 96, 045111 (2017).
- [46] A. Hariki, M. Winder, and J. Kuneš, Continuum charge excitations in high-valence transition-metal oxides revealed by resonant inelastic X-ray scattering, Phys. Rev. Lett. 121, 126403 (2018).
- [47] A. Hariki, M. Winder, T. Uozumi, and J. Kuneš, LDA + DMFT approach to resonant inelastic X-ray scattering in correlated materials, Phys. Rev. B 101, 115130 (2020).
- [48] M. Winder, A. Hariki, and J. Kuneš, X-ray spectroscopy of the rare-earth nickelate LuNiO₃: LDA+DMFT study, Phys. Rev. B 102, 085155 (2020).
- [49] Z. Hu, H. von Lips, M. S. Golden, J. Fink, G. Kaindl, F. M. F. de Groot, S. Ebbinghaus, and A. Reller, Multiplet effects in the Ru L_{2,3} x-ray-absorption spectra of Ru(IV) and Ru(V) compounds, Phys. Rev. B 61, 5262 (2000)
- [50] The similarity of the L- and M-edge is not surprising since they both correspond to p-d excitations, which are different only by core-valence interaction strength.
- [51] J. Okamoto, T. Okane, Y. Saitoh, K. Terai, S.-I. Fujimori, Y. Muramatsu, K. Yoshii, K. Mamiya, T. Koide, A. Fujimori, Z. Fang, Y. Takeda, and M. Takano, Soft X-ray magnetic circular dichroism study of Ca_{1-x}Sr_xRuO₃ across the ferromagnetic quantum phase transition, Phys. Rev. B 76, 184441 (2007).
- [52] We drop the \hat{z} subscript in $T_{\hat{z}}^{\pm}$ for sake of readability.

Supplementary Material to "X-ray Magnetic Circular Dichroism in RuO₂"

A. Hariki, ¹ Y. Takahashi, ¹ and J. Kuneš²

¹Department of Physics and Electronics, Graduate School of Engineering, Osaka Metropolitan University, 1-1 Gakuen-cho, Nakaku, Sakai, Osaka 599-8531, Japan ²Institute for Solid State Physics, TU Wien, 1040 Vienna, Austria

I. XMCD SIMULATION FOR RUO₂

We calculate Ru M- and L-edge X-ray absorption spectroscopy (XAS) and X-ray magnetic circular dichroism (XMCD) spectra using the LDA+DMFT Anderson impurity model (AIM) and the Ru⁴⁺ atomic model. Firstly, the LDA bands obtained with the WIEN2K package [1] for the experimental rutile structure [2] are projected onto a tightbinding model spanning Ru 4d bands, encompassing both the Ru t_{2g} and e_g states [3, 4]. The multi-band Hubbard model is defined by incorporating local electron-electron interaction within the Ru 4d shell to the tight-binding Hamiltonian. The electron-electron interaction is parameterized by Hubbard $U = F_0$ and Hund's $J = (F_2 + F_4)/14$ parameters where F_0 , F_2 , and F_4 are the Slater integrals [5, 6]. We adopt U = 3.0 eV and J = 0.45 eV which yields an antiferromagnetic solution with a magnetic moment consistent with Ref. [7]. The chosen U value is slightly larger than that in Ref. [7] due to explicit treatment of the Ru $4d e_q$ states in the multi-band Hubbard model explicitly. While the inclusion of Ru $4d e_q$ states is not essential for describing the magnetic and electronic structure of the system, it proves crucial for the XMCD line shape. This is because an X-ray excited core electron can be absorbed into the Ru e_g orbitals, not just the t_{2g} orbitals. A standard LDA+DMFT calculation [8, 9] for the multi-band Hubbard model is performed, following the same implementation of Refs. [10, 11]. The continuous-time quantum Monte Carlo method with the hybridization expansion formalism [12–14] is employed to solve the auxiliary AIM in the DMFT self-consistent calculation. The valence spectral intensities and hybridization densities $\Delta(\omega)$ are computed on the real frequency axis after the self-energy is analytically continued using the maximum entropy method [15, 16]. Subsequently, the XMCD intensities are computed from the AIM with the LDA+DMFT hybridization densities $\Delta(\omega)$, where the Ru 2p (L-edge) or 3p (M-edge) core orbitals and core-valence interaction are included. The core-valence interaction and SOC parameters are estimated by an atomic Hartree-Fock calculation following Refs. [10, 11, 17]. The

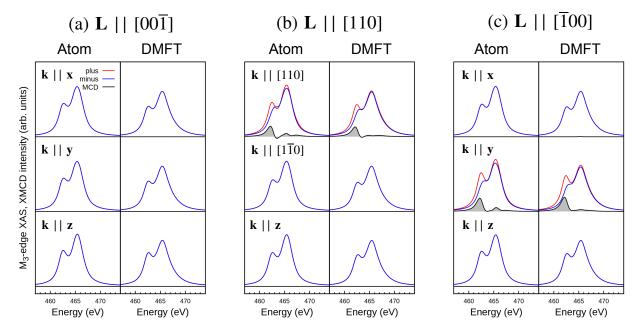


FIG. 1. Ru M_3 -edge XMCD spectra calculated by the Ru atomic model and the LDA+DMFT AIM model for for different orientation of the Néel vectors \mathbf{L} and x-ray wave vectors \mathbf{k} .

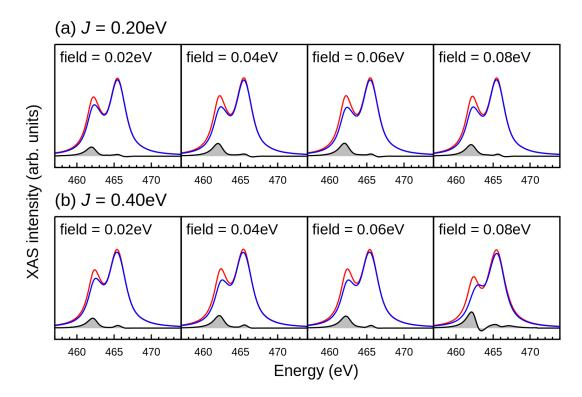


FIG. 2. Hund's J parameter and magnetic-field amplitude dependence of the M_3 -edge XMCD intensities calculated by the Ru atomic model. The calculations are performed for the Néel vector $\mathbf{L} \parallel [110]$ and x-ray wave vector $\mathbf{k} \parallel [110]$.

XAS spectral function is described by the Fermi's golden rule

$$F_{\rm XAS}^{(i)}(\omega_{\rm in}) = -\frac{1}{\pi} \operatorname{Im} \langle g | T^\dagger \frac{1}{\omega_{\rm in} + E_g - H_{\rm imp}^{(i)}} T | g \rangle.$$

Here, $|g\rangle$ is the ground with energy E_g , and $\omega_{\rm in}$ is the energy of the incident photon. T is the electric dipole transition operator for circularly-polarized X-rays [18, 19]. The index i = 1, 2 denotes the X-ray excited Ru site in the unit cell. The impurity Hamiltonian $H_{\rm imp}^{(i)}$ for each Ru site is used to calculate the individual site contribution, and the total XMCD intensities are obtained by summing up the contributions of two sites [11, 20].

Figure 1 shows the calcualted M_3 -edge XMCD intensities by the Ru⁴⁺ atomic model and the LDA+DMFT AIM model. The results from the atomic model closely resemble the LDA+DMFT AIM ones for all the studied Néel vectors \mathbf{L} and x-ray wave vectors \mathbf{k} . The amplitude of the Zeeman field and the Hund's coupling J in the atomic model is tuned to give rise to similar XMCD intensities of the LDA+DMFT AIM. Figure 1 demonstrates the validity of the use of a computationally-cheaper atomic model to analyze the optical conductivity tensors in the main text. Figure 2 presents the Hund's J and Zeeman field amplitude dependence of the XCMD intensities in the atomic model.

^[1] P. Blaha, K. Schwarz, G. Madsen, D. Kvasnicka, and J. Luitz, WIEN2k, An Augmented Plane Wave + Local Orbitals Program for Calculating Crystal Properties (Karlheinz Schwarz, Techn. Universitat Wien, Austria, 2001), ISBN 3-9501031-1-2.

^[2] T. Berlijn, P. C. Snijders, O. Delaire, H.-D. Zhou, T. A. Maier, H.-B. Cao, S.-X. Chi, M. Matsuda, Y. Wang, M. R. Koehler, P. R. C. Kent, and H. H. Weitering, Phys. Rev. Lett. 118, 077201 (2017).

^[3] A. A. Mostofi, J. R. Yates, G. Pizzi, Y.-S. Lee, I. Souza, D. Vanderbilt, and N. Marzari, Comput. Phys. Commun. 185, 2309 (2014).

^[4] J. Kuneš, R. Arita, P. Wissgott, A. Toschi, H. Ikeda, and K. Held, Comput. Phys. Commun. 181, 1888 (2010).

^[5] E. Pavarini, E. Koch, A. Lichtenstein, and D. E. Vollhardt, *The LDA+DMFT approach to strongly correlated materials*, Schriften des Forschungszentrums Jülich: Modeling and Simulation, Vol. 1 (2011) record converted from VDB: 12.11.2012.

^[6] E. Pavarini, "Electronic Structure Calculations with LDA+DMFT," in Many-Electron Approaches in Physics, Chemistry

- and Mathematics, Mathematical Physics Studies, ISBN 978-3-319-06378-2. Springer International Publishing Switzerland, 2014, p. 321, edited by V. Bach and L. Delle Site (2014) p. 321.
- [7] K.-H. Ahn, A. Hariki, K.-W. Lee, and J. Kuneš, Phys. Rev. B 99, 184432 (2019).
- [8] G. Kotliar, S. Y. Savrasov, K. Haule, V. S. Oudovenko, O. Parcollet, and C. A. Marianetti, Rev. Mod. Phys. 78, 865 (2006).
- [9] A. Georges, G. Kotliar, W. Krauth, and M. J. Rozenberg, Rev. Mod. Phys. 68, 13 (1996).
- [10] A. Hariki, T. Uozumi, and J. Kuneš, Phys. Rev. B **96**, 045111 (2017).
- [11] M. Winder, A. Hariki, and J. Kuneš, Phys. Rev. B 102, 085155 (2020)
- [12] P. Werner, A. Comanac, L. de' Medici, M. Troyer, and A. J. Millis, Phys. Rev. Lett. 97, 076405 (2006).
- [13] L. Boehnke, H. Hafermann, M. Ferrero, F. Lechermann, and O. Parcollet, Phys. Rev. B 84, 075145 (2011).
- [14] H. Hafermann, K. R. Patton, and P. Werner, Phys. Rev. B 85, 205106 (2012).
- [15] X. Wang, E. Gull, L. de' Medici, M. Capone, and A. J. Millis, Phys. Rev. B 80, 045101 (2009).
- [16] M. Jarrell and J. Gubernatis, Phys. Rep. 269, 133 (1996).
- [17] A. Hariki, M. Winder, T. Uozumi, and J. Kuneš, Phys. Rev. B 101, 115130 (2020).
- [18] M. Matsubara, T. Uozumi, A. Kotani, Y. Harada, and S. Shin, J. Phys. Soc. Jpn. 69, 1558 (2000).
- [19] F. de Groot and A. Kotani, Core Level Spectroscopy of Solids (CRC Press, Boca Raton, FL, 2014).
- [20] A. Hariki, T. Yamaguchi, D. Kriegner, K. W. Edmonds, P. Wadley, S. S. Dhesi, G. Springholz, V. Šmejkal, K. Výborný', T. Jungwirth, and J. Kuneš, "X-ray magnetic circular dichroism in altermagnetic α-MnTe," (2023), arXiv:2305.03588.